Sensors and Actuators A 205 (2014) 133–142

Contents lists available at ScienceDirect

Sensors and Actuators A: Physical

journal homepage: www.elsevier.com/locate/sna

A microfabricated shear sensor array on a chip with pressure gradient calibration

Zhengxin Zhao[a], Minchul Shin[a], Judith M. Gallman[b], Robert D. White[a,*]

[a] Mechanical Engineering, Tufts University, 200 College Avenue, Medford, MA 02155, USA
[b] Spirit Aerosystems, 3801 S. Oliver Street, Wichita, KS 67210, USA

ARTICLE INFO

Article history:
Received 16 April 2013
Received in revised form 15 October 2013
Accepted 2 November 2013
Available online 20 November 2013

Keywords:
Micromachined
Shear
Sensor
Floating element
Array
Pressure gradient

ABSTRACT

A micromachined floating element array sensor was designed, fabricated, and characterized. The sensor chip is 1 cm^2 and includes 16 separate sensor groups in a 4 by 4 array with a pitch of approximately 2 mm. The device was fabricated using four layers of surface micromachining including copper and nickel electroplating. A capacitance to digital converter IC was used to measure the differential capacitance change resulting from flow forces. The achieved resolution is limited by white noise with a level of 0.24 Pa/$\sqrt{}$Hz, and linearity is demonstrated to >13 Pa. Experimental characterization in three different duct height laminar flow cells allowed independent determination of the sensitivity to shear stress and pressure gradient. The sensor chip with half the elements acting in parallel has a sensitivity of 77.0 aF/Pa to shear and −15.8 aF/(Pa/mm) to pressure gradient. Pressure gradient sensitivity is found to be an important contributor to overall output, and must be accounted for when calibrating floating element shear stress sensors if accurate measurements are to be achieved. This work is the first demonstration of a shear sensor array on a chip with independent pressure gradient sensitivity calibration.

1. Introduction

The measurement of wall shear stress is important in many flow testing and device applications. Examples include drag measurements on air, space, land, and oceangoing vehicles both in test environments such as wind tunnels and in operation, as well as applications in active flow control. The measurement of surface shear stress is also important in industrial flow applications for fluid handling and manufacturing operations such as extrusion, and for biomedical devices in such applications as tissue engineering, where tissue development may depend on local shear stress. Flow regimes of interest may be as diverse as subsonic and supersonic turbulent boundary layers, turbulent pipe flows, and laminar flow in microchannels. Both steady and unsteady shear forces are of interest, and for some applications, particularly in turbulent boundary layer flows for aeroacoustic and structural acoustic applications, it may be important to capture the fluctuating shear stresses as well as the mean. Ideally, in order to capture the fine structure of turbulence, this would be done with a high spatial resolution on the order of 100 μm or smaller, and with high temporal resolution on the order of 1 ms or less [1–3].

A number of techniques exist for measuring surface shear stress. These include oil film interferometry [4], heated patch or heated wire measurements [5–7], hair-like sensors [8–10], surface fence measurements [11,12], and floating element techniques (see below). These techniques have been reviewed in a number of excellent papers and have various advantages and disadvantages [1,2,13–15].

Microelectromechanical system (MEMS) floating element sensors are one approach to the measurement of wall shear stress. In this measurement technology, a micromachined plate or shuttle is suspended using micromachined beam tethers. Under the influence of hydrodynamic forces, this "floating element" experiences a lateral deflection. The motion may be detected using capacitance change, piezoresistance, or optical methods. MEMS floating elements have the advantages of ease of use, high spatial and temporal resolution, and are a "direct" measurement technology insofar as they respond to momentum transfer at the wall. However, MEMS floating element sensors suffer from some drawbacks, including sensitivity to pressure gradients, potential for misalignment, and a possible lack of robustness to water or particle impingement [1–3].

A number of authors have described these devices in the past. The earliest work on MEMS floating elements is that of Schmidt et al. in 1988 [16]. Between 1995 and 1997, major contributions were made by Padmanabhan et al. with the introduction of optical detection methods [17–19]. Using optical detection, a resolution of 1 mPa was reported, although most testing occurred at levels

* Corresponding author. Tel.: +1 617 627 2210.
E-mail address: r.white@tufts.edu (R.D. White).

0924-4247/$ – see front matter © 2013 Elsevier B.V. All rights reserved.
http://dx.doi.org/10.1016/j.sna.2013.11.002

below 1 Pa. A single point was recorded by the research group demonstrating linearity to 10 Pa.

Pan et al., Hyman et al., and Patel et al. used capacitive sensing for three different related designs that included on-chip electronics and force rebalancing [20–22]. Linear response was demonstrated out to 4 Pa for the first two designs. The third design is the largest maximum demonstrated linear response in the literature, maintaining linear response out to approximately 25–30 Pa of effective shear stress.

In more recent work, Zhe et al. used differential capacitive measurements in a cantilever structure, and focused on high resolution at low stress levels [23], achieving 0.04 Pa resolution at stresses up to 0.2 Pa. Chandreskaran et al. also used differential capacitive measurement focusing on unsteady shear stress measurement [24,25], and were able to demonstrate 15 μPa/Hz$^{1/2}$ resolution at 1 kHz with linear response up to 2 Pa. Notable work by Barlian et al. [26] and Shajii et al. [27] describe piezoresistive floating elements for measurement in liquids.

Significantly, the majority of MEMS sensors so far described in the literature for measurement in air have either not been calibrated, or not shown linear response, at shear stress levels above 4 Pa, yet average shear stresses on the order of 50 Pa or higher may be routinely encountered in typical air vehicle flow applications. For instance, at a free stream velocity of approximately 250 m/s (Mach 0.8), typical of commercial air liners, in air with sound speed 300 m/s, at a density of 0.4 kg/m^3 and a viscosity of 1.5×10^{-5} Pa s (approximate properties at a cruise altitude of 10 km), the Reynolds number is 7×10^6 based on a 1 m length scale (for example, 1 m down a flat plate). At these conditions, the 1/7th power law skin friction coefficient correlation [28] may be used to approximate the skin friction,

$$C_f = \frac{0.027}{Re_x^{1/7}} = \frac{\tau_w}{0.5\rho U^2} \quad (1)$$

where C_f is the skin friction coefficient, Re_x is the Reynold's number based on distance down a flat plate, τ_w is the wall shear stress, ρ is the density of air and U is the free stream velocity. This results in a C_f of 0.003 at 1 m from the leading edge, equivalent to a wall shear stress of 40 Pa for the above conditions. A location 1 m from the leading edge is selected as an example location; shear will vary over the body. It is emphasized that this is an estimate only; Eq. (1) is an incompressible friction factor for a turbulent boundary layer on a flat plate with zero pressure gradient. Compressibility effects at high subsonic Mach numbers will reduce the friction factor by approximately 10% [28], assuming there is not a great deal of heat transfer from the wall to the flow. These results are consistent with recent oil film measurements on a 2.7% scale model of a commercial airliner, the common research model, conducted in the NASA Ames 11 foot transonic tunnel under similar Mach and Reynold's number conditions to those experience in commercial flight. Measured values of C_f on the majority of the wing, tail, and body varied from approximately 0.002 to 0.004 [29].

In this paper we describe a floating element sensor array on a chip that has been calibrated to high shear levels, and also characterized in an effort to directly determine the sensitivity to streamwise pressure gradients. The sensor uses a differential capacitive sensing modality, and is configured mechanically in a folded beam floating element structure. The structure differs from previous devices in a number of ways. First, micromachined bumps are included on the sensor surface in an effort to increase sensitivity. Secondly, the chip includes 16 separately addressable sensors, which increases system robustness and opens the possibility of measurement of the spatial variation of shear with approximately 2 mm spatial resolution. Third, the sensor is fabricated in a low cost and easily implemented nickel on glass fabrication process that does not require deep etching or bonding steps. Finally, a direct capacitance to digital readout chip, the AD7747 [Analog Devices, Wilmington, MA], is used for high resolution differential measurement of capacitance that can be transmitted digitally over long distances with no concerns regarding shielding.

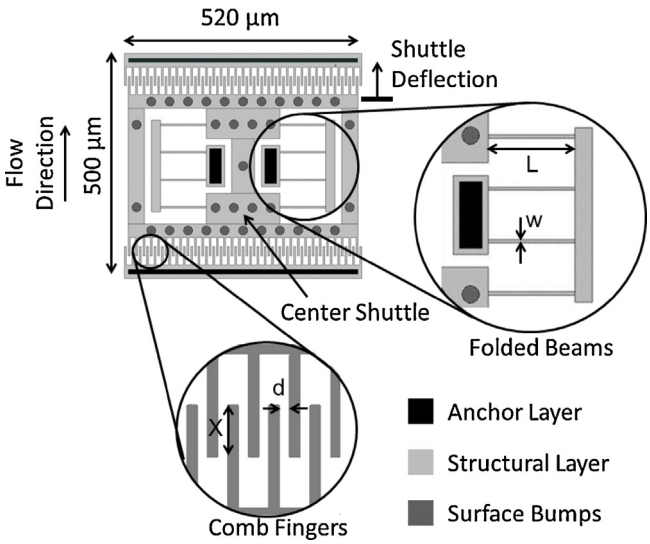

Fig. 1. Diagram of the mechanical structure of the floating element sensor.

In an effort to extend the operational range toward high shear stresses, the sensor has been calibrated and shows linear response up to 13 Pa in laminar flow. Patel et al. and Padmanabhan et al. are the only works of which we are aware that shows linear results above 4 Pa. Patel demonstrates linear calibration results up to 25 Pa, but these calibrations are done in transitional and turbulent flows, and make assumptions about the effects of pressure gradient based on a simple mechanical model without experimental verification [22]. Padmanabhan performs the majority of his calibrations below 1 Pa, including a single point at 10 Pa, but with no description of the calibration method used for the high stress result [18].

In order to address important concern regarding the sensitivity of floating element sensors to pressure gradients, the sensor described in this paper has been tested in three laminar duct flow configurations, allowing separate experimental determination of the sensitivity to pressure gradient and shear stress. The pressure gradient sensitivity in these flow fields was found to be substantial, contributing approximately as much force on the structure as the surface shear. This appears to be a very important effect that should be considered whenever calibration of a MEMS floating element sensor is attempted. As far as we are aware, this paper gives the first result experimentally distinguishing these two sensitivities for a MEMS floating element sensor.

2. Design

2.1. Electromechanical modeling

The design of an individual floating element sensor in the array, shown in Fig. 1, has many similarities to the sensor described in [21]. Each element has a movable center shuttle which experiences forces from interaction with the flow, two sets of comb fingers for differential capacitive sensing of the motion of the shuttle, and a series of folded beams to act as an elastic support. The four inner beams and the outer fingers are fixed on the substrate through the anchors. A folded beam structure is employed to reduce the effects of residual stresses introduced during manufacturing. The dimensions of the element are given in Table 1.

Table 1
As-manufactured dimensions of the floating element sensor.

Finger gap, d (μm)	2.88
Finger width (μm)	5.13
Number of comb fingers on the shuttle, N	64
Thickness of structure, t (μm)	8.8
Width of folded beam, w (μm)	5.13
Length of folded beam, L (μm)	99.2
Height of bump (μm)	11.7
Diameter of bump (μm)	24.7
Height of air gap below shuttle (μm)	5.2
Shuttle top area, A_m (mm^2) *(includes finger and shuttle top surface area)*	0.085

Flow forces acting on the center shuttle will bend the folded beams and create shuttle displacement primarily in the direction of maximum beam flexibility, shown in the figure, which is nominally aligned with the flow. Considering the shuttle and the fingers as a rigid body, the sensor stiffness in the lateral in-plane direction is easily related to the geometry of the beams [21]

$$K_x = 2Et\left(\frac{w}{L}\right)^3 \tag{2}$$

where E is the Young's modulus of the structural material (Nickel), and w, t, and L are the width, thickness and length of each beam, as shown in Fig. 1. Here K_x is the net stiffness of the entire folded beam structure acting in parallel. The aspect ratio (t to w) should be high to reduce out-of-plane motion.

Interdigitated overlap of the comb fingers determines the total active capacitance of the element,

$$C = 2N\frac{\varepsilon t}{d}X \tag{3}$$

where N is the number of fingers attached to the shuttle, ε is permittivity of air, t is the thickness of the structure, d is the finger gap and X is the overlap length. Eq. (3) ignores capacitive fringing effects at the edges and assumes no out-of-plane motion. Given this, the differential change of capacitance for the element depends on the displacement δX only,

$$\delta C = 2N\frac{\varepsilon t}{d}\delta X \tag{4}$$

The sensitivity of the floating element to a constant applied force, in terms of capacitance change, is thus

$$S_1 = \frac{\partial C}{\partial F} = \frac{\partial C}{\partial X}\frac{\partial X}{\partial F} = \frac{\partial C}{\partial X}\frac{1}{K_x} = \frac{N\varepsilon L^3}{Edw^3} \tag{5}$$

A dynamic model including mass loading and damping forces is not considered in this work, although such considerations are important for unsteady shear sensors and will need to be considered in future work.

2.2. Fluid forces

The structure will respond to forces applied to the shuttle arising from interaction with the flow field. For a perfectly smooth shear sensor with no gaps or topology, the lateral force would simply be the surface area of the shuttle multiplied by the wall shear stress. Thus, some previous authors have assumed that the static force on the sensor would be

$$F \approx A_m \cdot \tau_{yx} \tag{6}$$

where A_m is the physical top surface area of the sensor shuttle and τ_{yx} is the wall shear stress present at the wall. However, for a sensor that includes gaps, topology, roughness, and packaging topology, it is expected that the steady fluidic force may depend on both the time average local wall shear stress, the local streamwise pressure gradient in the flow, and the details of the geometry at the microscale. It is also possible that the compressibility of the flow may play a role, and, in the case of boundary layer flows, the boundary layer thickness may be important. A fully 3D numerical analysis coupled with a series of experiments is required to capture all the details of this interaction, as the local geometries are complex. Such an analysis is outside the scope of this paper, although it should be conducted in future work. The only numerical flow work for a floating element shear sensor of which we are aware is the conference paper by Chen and Reshotko [30]; more work needs to be done.

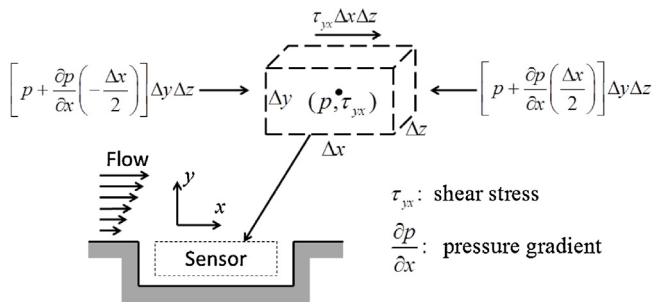

Fig. 2. Simple model of the flow interaction with the shear sensor including pressure gradient and surface shear.

As a first step toward a more comprehensive, but still experimentally tractable, flow interaction model, consider the sensor to have an effective rectangular shape, and to be acted on by the local surface shear stress and the pressure gradient present in the flow, as diagrammed in Fig. 2.

It is emphasized that the effective size of the element, Δx by Δy by Δz, is not identical to the physical size of the element. These effective dimensions will be determined experimentally, and, to first order, account for the unknown details of the microscale flow around the element. They can also account for small manufacturing nonuniformities or imperfect packaging, such as a slightly misaligned sensor. It is likely that these dimensions will be of the same order of magnitude as the physical size of the element. Given this model, the fluidic force acting on the element will be

$$F = \tau_{yx}\cdot\Delta x\Delta z - \left(\frac{\partial p}{\partial x}\right)\cdot\Delta x\cdot(\Delta y\Delta z) \tag{7}$$

By combining Eqs. (5) and (7), the differential sensitivity of a single element to the two flow variables can then be written

$$S_2 = \frac{\partial C}{\partial \tau_{yx}} = \frac{\partial C}{\partial F}\frac{\partial F}{\partial \tau_{yx}} = \frac{N\varepsilon L^3}{Edw^3}\Delta x\Delta z \tag{8}$$

$$S_3 = \frac{\partial C}{\partial(\partial p/\partial x)} = \frac{\partial C}{\partial F}\frac{\partial F}{\partial(\partial p/\partial x)} = \frac{-N\varepsilon L^3}{Edw^3}\Delta x\Delta y\Delta z \tag{9}$$

where S_2 is the sensitivity to shear, and S_3 is the sensitivity to pressure gradient.

With this model in mind, in an effort to increase the sensitivity of the sensor by increasing the effective area of interaction with the flow (Δx, Δy, and Δz), surface bumps were fabricated on the top of the shuttle. As shown in Fig. 1, 35 cylindrical bumps, each 12 μm high with a diameter of 25 μm, were fabricated in a distributed pattern.

2.3. Array

In anticipation of a future goal of measuring local spatial variation in unsteady shear, the 1 cm square chip was designed to include an array of 16 by 16 elements. The 256 elements were subdivided into 16 groups of 16 elements each, so that each group has a 4 by 4 pattern of elements as shown in Fig. 3.

Each group has independent connections routed to three electrical pads for the top combs, bottom combs, and common (center

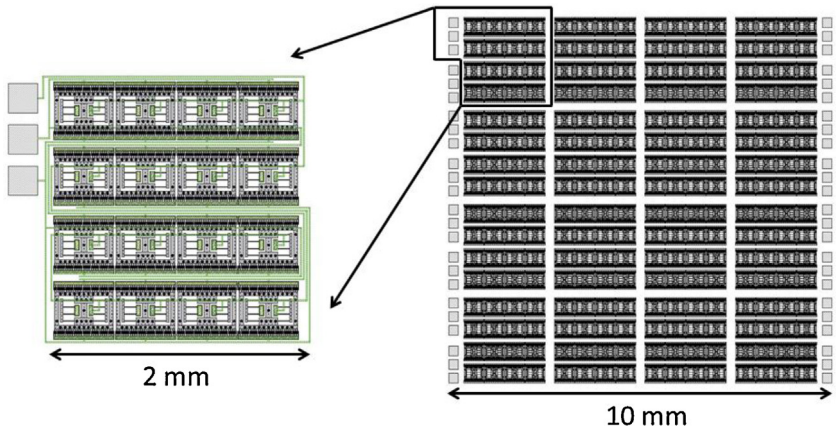

Fig. 3. Layout of the 1 cm^2 array chip. 256 elements are arranged into 16 groups of 16 elements. Each group is independently addressable.

shuttle) electrodes. The groups are approximately 2 mm × 2 mm in size, thus the spatial resolution for shear measurements of the array-on-a-chip is on the order of 2 mm. The local shear stress of a group or average shear of the whole chip can be measured separately. This allows the end user to trade off between spatial resolution and sensitivity. In addition, a major benefit of the array architecture is that failure of a single element or single group, either during fabrication or during operation, does not destroy the functionality of the entire chip. This may be a highly desirable feature for sensors deployed in harsh operating environments where single elements may be lost to particulates or moisture, but the chip continues to function, albeit with reduced sensitivity.

3. Fabrication and packaging

The sensors were fabricated using a four-mask nickel surface micromachining process in the Tufts Micro/Nano Fab, shown in Fig. 4. The process started with a soda lime glass substrate of 550 μm thickness (step 1). In step 2, a two layer liftoff resist, LOR-20B [Microchem, Newton, MA], was deposited and patterned via lithography. 75 nm/250 nm thick Cr/Au interconnects were sputtered on, followed by liftoff (step 3). Subsequent to this, in steps 4 and 5, a seed layer of Ti/Cu (30 nm/300 nm) was deposited and patterned using an identical liftoff process. The liftoff resist uses a two layer process to create a reentrant photoresist profile. Compared to traditional single layer liftoff, this method prevents the formation of raised ridges at the edges of the patterns and generation of metal particles. Next, in step 6, a thick photoresist layer was patterned to form anchor regions to the substrate, and an oxygen plasma descum was performed. A 5 μm sacrificial layer of copper was then electroplated on top of the seed layer to cover the entire substrate except the anchor regions. Plating was done using a commercial copper sulfate plating solution [Technic Inc., Cranston, RI] at room temperature. Care was taken to minimize the surface roughness by controlling the plating current and brightener percentage as well as agitating and continuously filtering the plating solution. For a plating current density of 5 mA/cm^2 and a total 5 μm thickness of copper, the RMS surface roughness is between 50 nm and 150 nm.

Subsequently, a 9 μm height floating element layer and a 12 μm height bump layer were electroplated in two steps using a commercial Nickel Sulfamate [Technic Inc., Cranston, RI] plating solution. As shown in step 7, the pattern was first established using a thick photoresist and descumed in an oxygen plasma. A brief acid etch was conducted to remove any copper oxide, and then Nickel was plated at 50 °C at 5 mA/cm^2 with a deposition rate of approximately 100 nm/min (step 8). The surface roughness of the nickel after plating is 150–200 nm. The roughness appears to be a reflection primarily of the roughness of the Cu sacrificial layer. Steps 9 and 10 were performed identically to steps 7 and 8 to produce the plated nickel bumps.

Finally, a protective photoresist layer was spun on for dicing. After dicing, the sacrificial copper layer was etched away in a mixture of 1 part Acetic Acid to 1 part 30% Hydrogen Peroxide to 18 parts DI water for 24 h. The chip was rinsed in water, Isopropanol, and Methanol, and allowed to air dry in a dry box that has been flooded with clean dry air with a low relative humidity. SEM images in Fig. 5 show the released structure. The as manufactured dimensions shown in Table 1 were taken from the SEM images for in-plane dimensions and from white light interferometry measurements for layer thicknesses.

After releasing, the sensors were packaged into a 4 cm by 4 cm ceramic pin grid array hybrid package (CPGA). First, the CPGA cavity was partially filled with potting epoxy [Namics Chipcoat G8345-6] which was then cured. The epoxy was CNC milled to the appropriate height, including a small square pocket to center and align the chip. The chip was mounted into the pocket with a thin epoxy film. The package was then ball bonded to the chip using 25 μm diameter gold wire. Finally, the wirebonds were potted in epoxy, which was allowed to settle and cure, with multiple layers being applied until a flat surface was achieved around the chip and package. Using this method, it was possible to create a flat surface with a total maximum topology from the ceramic surface, onto the epoxy, over the wirebonds and onto the chip of approximately 0.1 mm. Fig. 6 shows a photograph of the packaged chip, and a stylus profilometer scan of the surface topology from the package, onto the epoxy, across the wirebonds, onto the chip and back onto the package. As can be seen, the packaging exhibits approximately 0.1 mm of total topology, and the chip is parallel to the package surface within 0.1°.

4. Experimental methodology

4.1. Flowcell

The floating element sensor was tested in a laminar flowcell, similar to that described by other authors [20]. A duct flow channel was created by CNC milling a thin rectangular slot into an aluminum plate, and assembling this with a flat bottom plate with a square cutout for flush mounting the package. The slot is 28 mm wide. Three different height slots were used, h_f = 0.30, 0.40 and 0.53 mm. The inlet air supply was house clean dry air, and was regulated via computer control using a digital flow controller, Omega FMA3812 [Omega Engineering, Stamford, CT]. This unit controls the total

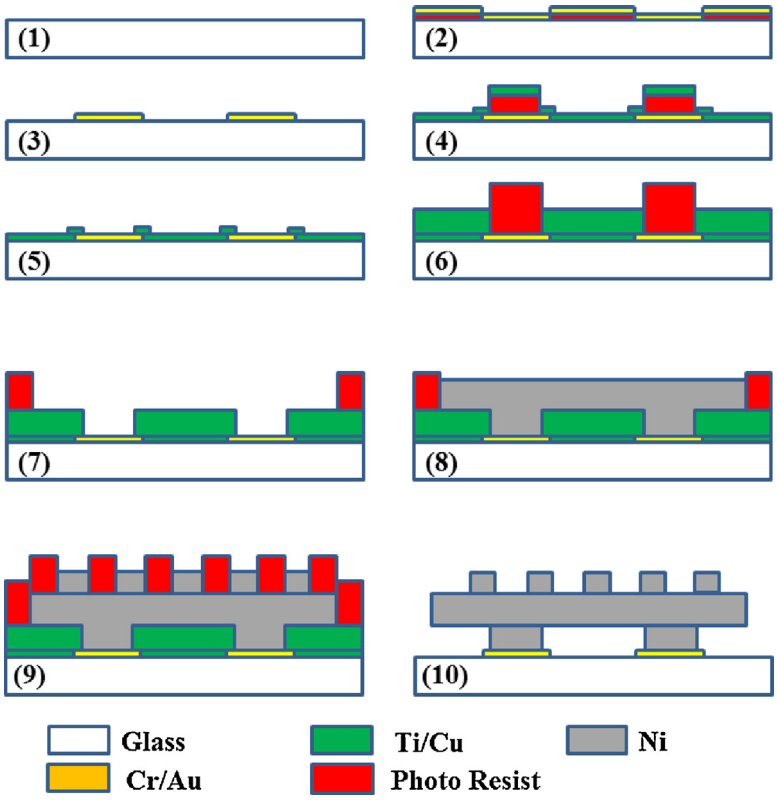

Fig. 4. Nickel-on-glass fabrication process. Ti/Cu is used as a sacrificial layer.

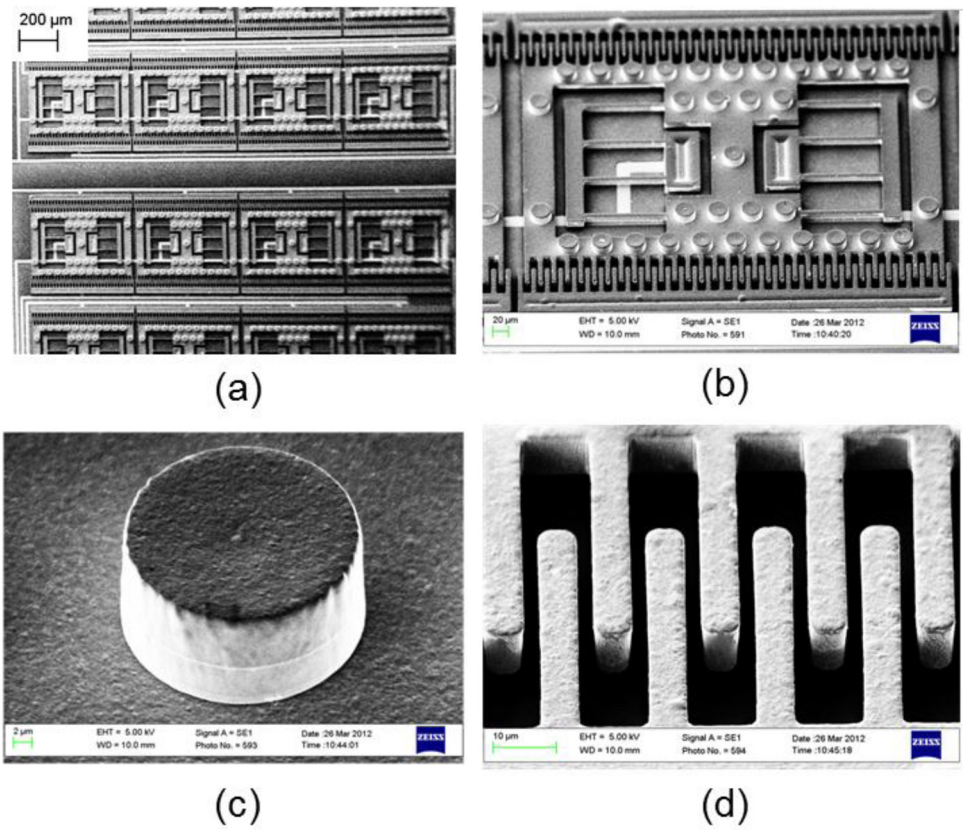

Fig. 5. SEM images of a released sensor chip. (a) Multiple elements in one group, (b) a single element, (c) a bump and (d) comb fingers.

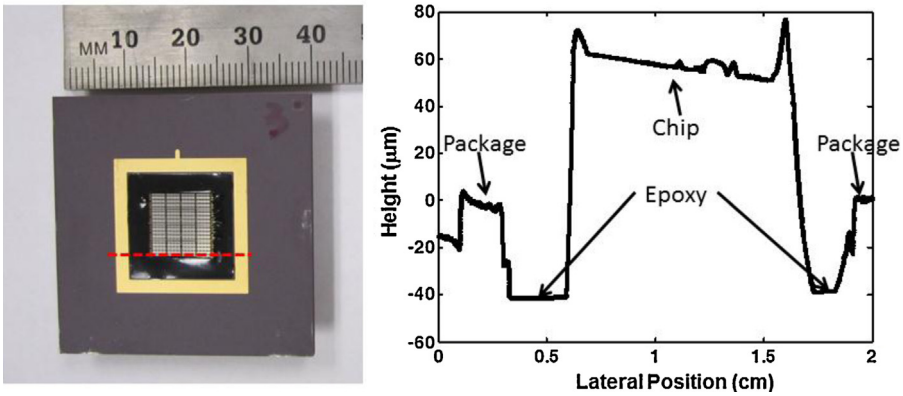

Fig. 6. (Left) A finished sensor chip packaged and potted in a ceramic pin grid array package. A dashed line indicates the line along which a stylus profilometer scan was taken. (Right) The measured height of the surface topology along the indicated scan line.

volume flow rate from 0 to 40 cubic feet per hour (CFH). The outlet flow exits to atmosphere. Fig. 7 is a diagram of test setup.

Five static pressure taps were included on the top of the channel along the streamline, with a pitch of 12.7 mm, to measure the pressure gradient in the fully developed region. The fifth pressure tap was located directly above the sensor. The static pressure was measured using an Omega PX209 pressure transducer [Omega Engineering, Stamford, CT]. Care was taken to ensure that the flow cell was long enough that the flow was fully developed before reaching the pressure taps or the device under test. For flow rates of 40 CFH or less, the flow in the duct was laminar, and so the flow can be described by a Poiseuille flow profile for a narrow slot [28],

$$u(y) = \frac{6Q}{b_f h_f}\left(\frac{1}{4} - \left(\frac{y}{h_f}\right)^2\right) \tag{10}$$

where Q is the volume flow rate, $b_f = 28$ mm is the duct width, $h_f = 0.3$, 0.4 or 0.5 mm is the duct height, and $y = -h_f/2 \ldots h_f/2$ is the coordinate. At $Q = 3.15 \times 10^{-4}$ m^3/s (40 CFH), for the smallest duct, the centerline velocity is 56 m/s, resulting in a centerline Mach number of 0.16 and an area averaged Mach number of 0.11. Hence, even at the highest flow rates, the flow can be considered incompressible.

The Reynold's number based on the average flow velocity and hydraulic diameter is

$$Re_{D_h} = \frac{2\bar{u}\rho h_f}{\mu} = \frac{2Q\rho}{b_f \mu} \tag{11}$$

which does not vary with duct height. At the maximum flow rate of $Q = 3.15 \times 10^{-4}$ m^3/s (40 CFH), using $b_f = 28$ mm, $\mu = 1.8 \times 10^{-5}$ Pa s, and $\rho = 1.2$ kg/m^3, $Re_{D_h} = 1500$ [28]. Transition to turbulence in parallel plate flow occurs above a Reynolds number of 2000 [28], thus the flow is expected to remain laminar, for all duct heights, up to the highest flow rate tested.

Given this, the pressure gradient and wall shear stress are expected to be

$$\frac{\partial p}{\partial x} = \frac{-12\mu Q}{h_f^3 b_f} \tag{12}$$

and

$$\tau_{yx} = \frac{-1}{2} h_f \left(\frac{dp}{dx}\right) = \frac{6\mu Q}{h_f^2 b_f} \tag{13}$$

The measured pressure gradient is shown in Fig. 8, and exhibits excellent agreement with the expectations of Eq. (12), giving considerable confidence that the flow is fully developed and laminar, and that the shear stress of Eq. (13) is accurate. Since pressure gradient and shear stress scale as h_f^{-3} and h_f^{-2} respectively, it is possible to produce laminar flow regimes with linearly independent values of the two fluid forcing terms by varying the duct height. Advantage will be taken of this fact to independently determine the two sensitivities, S_2 and S_3.

4.2. Electronics

A schematic of the system electronics is shown in Fig. 9. An AD7747 [Analog Devices, Wilmington, MA] capacitance to digital converter chip was used to measure the differential capacitance between the top and bottom electrodes on the MEMS chip. The chip uses an AC excitation and a sigma delta modulator to measure differential capacitance changes of ±8 pF, and is capable of removing offset static differential capacitances as high as 17 pF. On chip registers control the conversion rate, AC excitation level, and allow for nulling of any static capacitance offset. The best results in terms of noise performance were achieved using the slowest conversion rate of 219.3 ms, and an excitation voltage level of $\pm 3/8 \times V_{DD}$, which produces a voltage swing from 0.625 V to 4.375 V applied to the MEMS capacitors. With these settings the AD7747 was expected to provide a resolution of 9.0 aF/$\sqrt{}$Hz according to the datasheet [31].

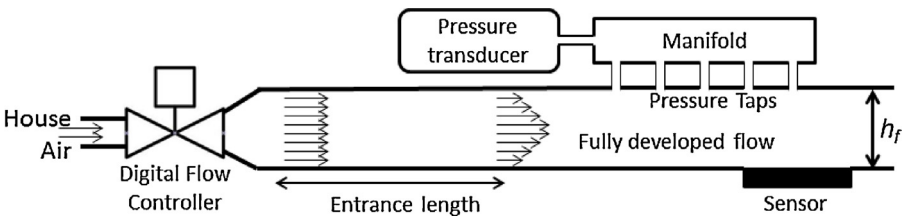

Fig. 7. Diagram of the laminar flow cell test apparatus.

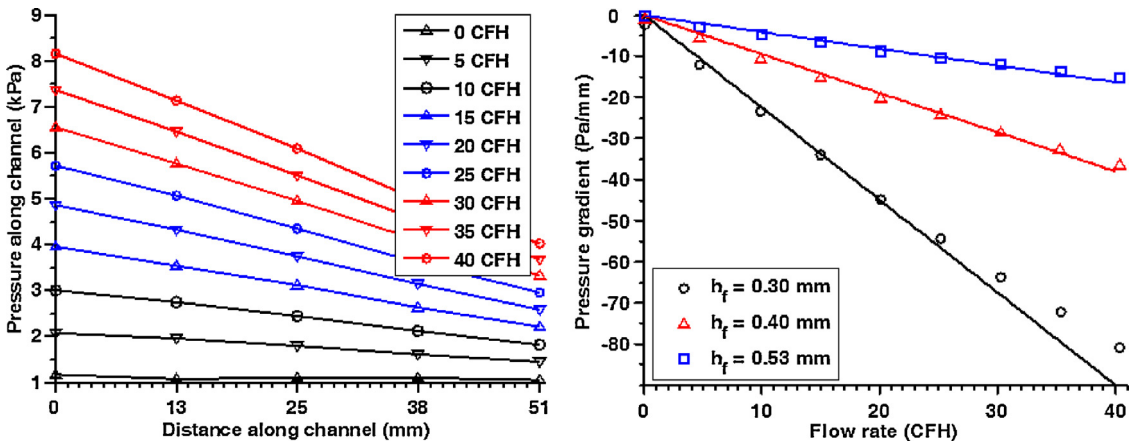

Fig. 8. (Left) Measured pressure as a function of distance down the duct for different flow rates in the h_f = 0.30 mm high duct. (Right) Measured pressure gradient as a function of flow rate (symbols) compared to the Poiseuille flow model (lines), Eq. (12), plotted for the three duct heights.

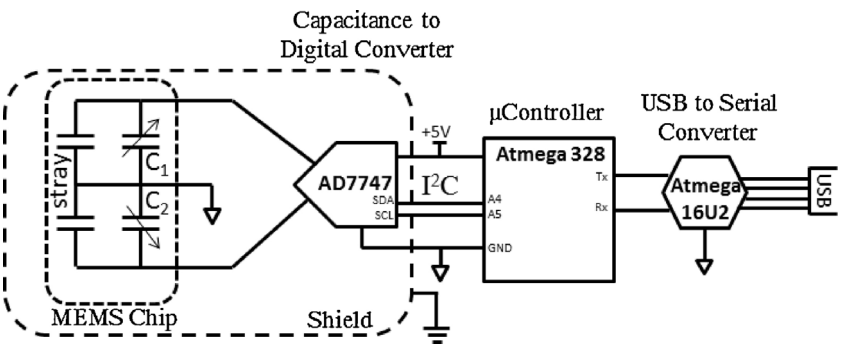

Fig. 9. Readout electronics used an AD7747 capacitance to digital converter to perform differential capacitance measurements on the MEMS chip. Communication was via I^2C to a microcontroller which then communicates over USB.

Analog to digital conversion happens at the AD7747, which is located as close as possible to the MEMS chip and enclosed in a grounded shield. This helps to reduce electromagnetic interference (EMI). Once conversion happens, the signal is digital and immune to EMI. The AD7747 communicates with an Atmega328 microcontroller using the two wire I^2C protocol. The microcontroller then communicates with a computer over USB via an Atmega16U2 configured as a serial to USB converter. The speed of the system is limited by the conversion time of the AD7747. Shorter conversion times down to 22 ms can be used, but result in a lower capacitance resolution.

5. Results

The packaged sensor chip was tested in the laminar flow cell at each of the three duct heights. For the tests presented here, 8 of the 16 groups on the chip were connected in parallel, so the output is the total capacitance change from 128 elements. Before each test, the electronics were turned on for 2 h with no flow, and then the flow was turned on at 10 CFH for an additional 2 h. This conditioning was found to remove startup transients that were otherwise observed. The startup transients appear to be related to ambient temperature and humidity, as well as surface charging of the glass, but the mechanisms are not well known. More work is needed to determine the source of startup transients and eliminate them. Hysteresis was not observed experimentally.

After the 4 h turn on and soak, the flow rate was controlled by the computer via the digital flow controller starting at 0 flow rate, and increasing to 40 CFH in steps of 5 CFH. Each flow rate was held for 60 s. The first 30 s at each condition were not integrated, to allow the flow and sensor to settle. The differential capacitance measured during the second 30 s was used for computing the average and standard deviation of the capacitance change at that flow rate. As mentioned previously, a conversion rate of 219.3 ms was used on the AD7747. Additional communications overhead resulted in 2.94 capacitance samples per second. A typical result is shown in Fig. 10.

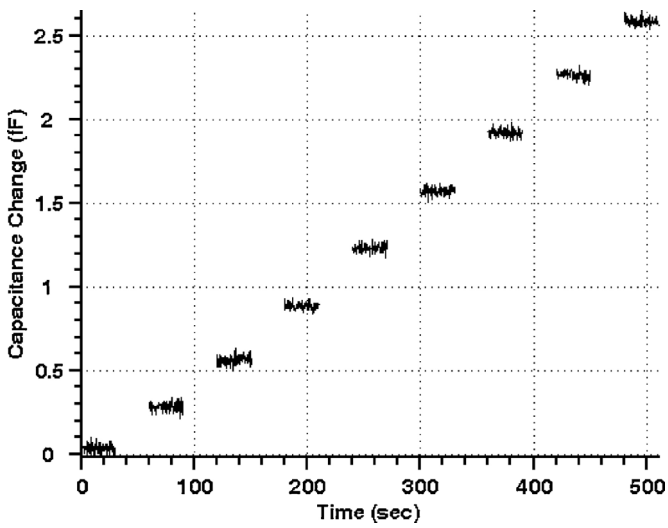

Fig. 10. Measurement of the change in capacitance of 8 groups on the MEMS chip during flow testing in the 0.30 mm high flow duct. Each step in capacitance corresponds to a 5 CFH increase in flow rate, from 0 to 40 CFH.

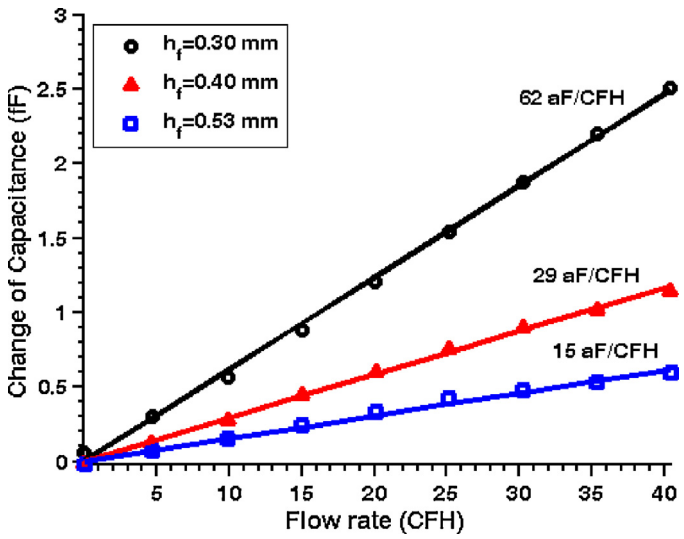

Fig. 11. Measured change in capacitance vs. flow rate for all three channel heights. Best-fit lines are also shown.

Fig. 11 shows the average change in capacitance as a function of the flow rate for the three different channel heights. This average is computed for the 30 s of data at each stabilized flow rate. Since the data rate is 2.94 samples/s, there are 90 measured values at each flow rate.

The standard deviation of the capacitance about the mean for the time domain data gives the noise density of the measurement. For all data measured in the 0.30 mm high duct, the standard deviation was 22.1 aF. A plot of the power spectral density of the capacitance noise shows that it is white noise. Hence, the noise density of the measurement is related to the standard deviation by

$$P_x = \sqrt{\frac{2\sigma^2}{F_s}} \tag{14}$$

where P_x is the noise density in aF/$\sqrt{}$Hz, σ is the standard deviation in aF, and F_s = 2.94 is the sample rate in samples/second. The noise density of the capacitance measurement is therefore 18.2 aF/$\sqrt{}$Hz at low frequencies (below 1.5 Hz). This is approximately double, but on the same order, as the typical noise of the unloaded AD7747 given on the datasheet, 9.0 aF/$\sqrt{}$Hz. The reduction in resolution could be due to loading effects on the AD7747, EMI, real fluctuations in flow rate, or thermal-mechanical noise of the floating element.

Using the sensitivity model given in Eqs. (8) and (9), it is postulated that the change in capacitance can be related to the shear stress and pressure gradient by

$$\Delta C = S_2 \tau_{yx} + S_3 \frac{\partial P}{\partial x} \tag{15}$$

For each flow condition the pressure gradient and the shear stress are known, either from the flow rate according to Eqs. (12) and (13), or from direct measurement of pressure gradient. There are 24 non-zero flow conditions to evaluate and two constants to fit. This becomes a least squares problem; essentially we are fitting a plane to the data in shear stress-pressure gradient space. A linear least squares fit was performed to the 24 data points to determine the two sensitivities. It is emphasized that these sensitivities are for 8 groups of elements (128 individual elements) acting in parallel.

$$\begin{aligned} S_2 &= 77.0\,\text{aF/Pa} \\ S_3 &= -15.8\,\text{aF/(Pa/mm)} \end{aligned} \tag{16}$$

The norm of the residual is 56.6 aF, corresponding to 0.74 Pa of error. If, on the other hand, the pressure gradient sensitivity were neglected; that is, if we force S_3 = 0, then the best fit is S_2 = 173 aF/Pa. For this case, the norm of the residual is 434 aF, corresponding to 2.5 Pa of error. A comparison of the measured vs. actual wall shear stress is given in Fig. 12 for the two cases. Correcting for pressure gradient sensitivity improves the accuracy of the measurement.

6. Discussion

It is quite significant that correcting for pressure gradient sensitivity improves accuracy for these 3 flow cases, but the result has even greater importance than simply improving accuracy in laminar flow. If the sensor were to be used in a different flow regime, such as under a turbulent boundary layer with adverse or favorable pressure gradients, the substantial sensitivity to pressure gradient could cause inaccurate measurements of shear if neglected. For example, consider a flow measurement performed under a turbulent boundary layer with zero pressure gradient. If the actual wall shear were 10 Pa, but pressure gradient effects were neglected in the calibration, then the sensor would suggest that the wall shear was $(S_2/S_3)(10\,\text{Pa})$ = 4.4 Pa, a large error.

The experiments conducted in this work are not sufficient to demonstrate that the model of Eqs. (15) and (16) is sufficient for describing sensitivity to all kinds of flow, such as TBLs, turbulent duct flows, separated flows, or a variety of other flows of interest. However, these experiments do demonstrate that pressure

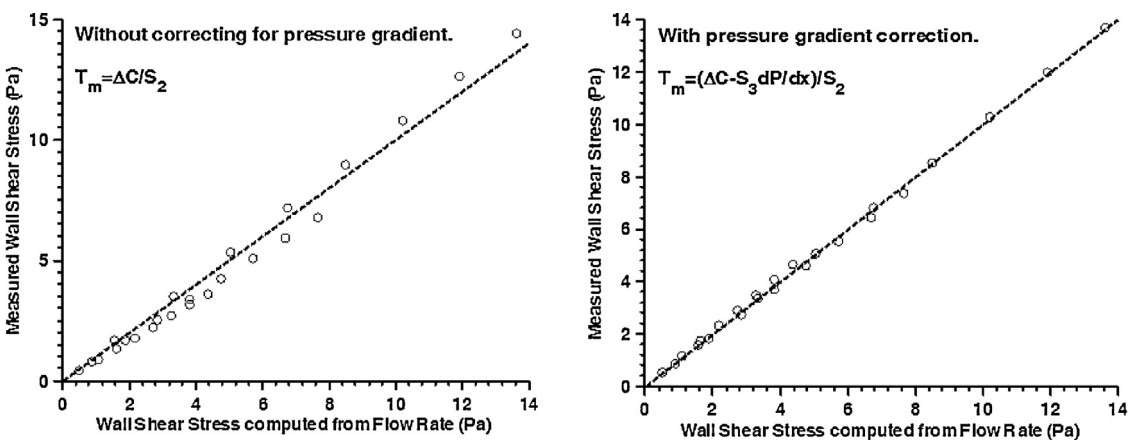

Fig. 12. Comparison of shear stress measured by the MEMS sensor (y-axis) to shear stress computed from the volume flow rate (x-axis). All 24 non-zero flow conditions are plotted as open circles. The dashed line is the unit line, indicative of an accurate measurement. The plot on the left assumes no pressure gradient sensitivity. The plot on the right corrects for the pressure gradient using the measured sensitivity as in Eqs. (15) and (16).

gradient effects are a necessary consideration in calibrating floating element sensors and should not be neglected.

With the measured sensitivities in hand, it is now possible to go back to the electromechanical model developed in Eqs. (8) and (9) to see what the effective surface area and effective volume of the element are. Keep in mind that there are 128 elements acting in parallel in the experiment, so the sensitivity will be 128 times that of Eqs. (8) and (9). Using the measured dimensions from Table 1, and taking the modulus of electroplated Nickel to be $E = 205$ GPa [32], the effective surface area of the element is

$$\Delta x \Delta z = \frac{Edw^3}{128 \cdot N\varepsilon L^3} S_2 = 0.086\,\text{mm}^2 \tag{17}$$

which is very close to the actual physical surface area of the shuttle, 0.085 mm^2. The effective volume of the element is

$$\Delta x \Delta y \Delta z = \frac{-Edw^3}{128 \cdot N\varepsilon L^3} S_3 = 1.8 \times 10^{-2}\,\text{mm}^3 \tag{18}$$

which is more than an order of magnitude larger than the physical volume of the shuttle, 7.5×10^{-4} mm^3. On this basis it is concluded that the element shows the sensitivity to surface shear that would be predicted based solely on the physical surface area, but considerably more sensitivity to pressure gradient than would be predicted based on the physical volume. It seems likely that the increase in pressure gradient sensitivity is due to two factors: (1) the complexities of the flow around the microscale geometries of the beams, combs, and bumps leading to changes in pressure close to the element features (2) the topology of the package contributing to changes in the flow pattern at the scale of the entire chip, resulting in changes to the fluidic forces.

It is important to determine the mechanisms that lead to the increased pressure gradient sensitivity. Initial two and three dimensional computational fluid dynamics results support the idea that flow around the edges of the element, the combs and the beams result in substantial increases in the pressure loading on the structure. It may be that decreasing the size of the gaps around structural elements such as the beam tethers can reduce pressure gradient sensitivity. However, additional analysis and experimental work is required to explore the mechanisms.

7. Conclusion

A unique array-based floating element shear stress sensor with surface bumps was developed with the ultimate goal of measuring local shear stress at small spatial scales. The chip includes 16 individually addressable groups in a 4 by 4 array with a spatial resolution of 2 mm. A capacitance to digital converter IC was used successfully to make digital differential capacitance measurements in laminar duct flows. Experiments conducted in three different height flow ducts allowed independent determination of the sensitivity to surface shear (77.0 aF/Pa) and pressure gradient (−15.8 aF/(Pa/mm)) for 8 groups (128 elements) acting in parallel. The noise density of the sensor is 0.24 Pa/$\sqrt{}$Hz at low frequencies (below 1.5 Hz). Pressure gradient sensitivity is higher by approximately an order of magnitude than would be expected based solely on the physical volume of the element. For surface shear sensors of this type, it is important to measure and include a correction for pressure gradient sensitivity in order to achieve accurate measurements of surface shear stress. Future work will include additional analysis of the fluid structure interactions through computational fluid dynamics simulations and experiments in other types of flow regimes. In addition, unsteady measurements and dynamic models will be developed, error sources, drift, hysteresis and environmental sensitivity will be investigated, and the capability to address individual array elements will be added to the electronics.

Acknowledgements

This work was supported by a contract from Spirit Aerosystems, Wichita, KS.

References

[1] M. Sheplak, L. Cattafesta, T. Nishida, C.B. McGinley, MEMS Shear Stress Sensors: Promise and Progress, 2004.
[2] J.W. Naughton, M. Sheplak, Modern developments in shear-stress measurement, Progress in Aerospace Sciences 38 (2002) 515–570.
[3] L. Lofdahl, M. Gad-el-Hak, MEMS-based pressure and shear stress sensors for turbulent flows, Measurement Science and Technology 10 (1999) 665–686.
[4] L. Tanner, L. Blows, A study of the motion of oil films on surfaces in air flow, with application to the measurement of skin friction, Journal of Physics E: Scientific Instruments 9 (1976) 194.
[5] B. Van Oudheusden, Silicon thermal flow sensors, Sensors and Actuators A: Physical 30 (1992) 5–26.
[6] L. Lofdahl, V. Chernoray, S. Haasl, G. Stemme, M. Sen, Characteristics of a hot-wire microsensor for time-dependent wall shear stress measurements, Experiments in Fluids 35 (2003) 240–251.
[7] E. Kälvesten, C. Vieider, L. Löfdahl, G. Stemme, An integrated pressure—flow sensor for correlation measurements in turbulent gas flows, Sensors and Actuators A: Physical 52 (1996) 51–58.
[8] C. Brucker, J. Spatz, W. Schroder, Feasability study of wall shear stress imaging using microstructured surfaces with flexible micropillars, Experiments in Fluids 39 (2005) 464–474.
[9] A. Dagamseh, R. Wiegerink, T. Lammerink, G. Krijnen, Towards a high-resolution flow camera using artificial hair sensor arrays for flow pattern observations, Bioinspiration and Biomimetics 7 (2012) 046009.
[10] J. Chen, Z. Fan, J. Zou, J. Engel, C. Liu, Two-dimensional micromachined flow sensor array for fluid mechanics studies, Journal of Aerospace Engineering 16 (2003) 85.
[11] R. Savelsberg, M. Schiffer, E. Obermeier, I.P. Castro, Calibration and use of a MEMS surface fence for wall shear stress measurements in turbulent flows, Experiments in Fluids 53 (2012) 489–498.
[12] T. von Papen, U. Buder, H.D. Ngo, E. Obermeier, A second generation MEMS surface fence sensor for high resolution wall shear stress measurement, Sensors and Actuators A: Physical 113 (2004) 151–155.
[13] K. Winter, An outline of the techniques available for the measurement of skin friction in turbulent boundary layers, Progress in Aerospace Sciences 18 (1979) 1–57.
[14] H. Fernholz, G. Janke, M. Schober, P. Wagner, D. Warnack, New developments and applications of skin-friction measuring techniques, Measurement Science and Technology 7 (1996) 1396.
[15] C. Ho, Y. Tai, Micro-electro-mechanical-systems (MEMS) and fluid flows, Annual Review of Fluid Mechanics 30 (1998) 579–612.
[16] M.A. Schmidt, R.T. Howe, S.D. Senturia, J.H. Haritonidis, Design and calibration of a microfabricated floating-element shear-stress sensor, IEEE Transactions on Electron Devices 35 (1988) 750–757.
[17] A. Padmanabhan, H. Goldberg, K. Breuer, M. Schmidt, A silicon micromachined floating-element shear-stress sensors with optical position sensing by photodiodes, in: 8th International Conference on Solid State Sensors and Actuators, and Eurosensors IX, 1995.
[18] A. Padmanabhan, M. Sheplak, K. Breuer, M. Schmidt, Micromachined sensors for static and dynamic shear-stress measurements in aerodynamic flows, in: International Conference on Solid State Sensors and Actuators, TRANSDUCERS'97 Chicago, 1997, pp. 137–140.
[19] A. Padmanabhan, H. Goldberg, K.D. Breuer, M.A. Schmidt, A wafer-bonded floating-element shear stress microsensor with optical position sensing by photodiodes, Journal of Microelectromechanical Systems 5 (1996) 307–315.
[20] D. Hyman, T. Pan, E. Reshotko, M. Mehregany, Microfabricated shear stress sensors, part 2: testing and calibration, AIAA Journal 37 (1999) 73–78.
[21] T. Pan, D. Hyman, M. Mehregany, E. Reshotko, S. Garverick, Microfabricated shear stress sensors, part 1: design and fabrication, AIAA Journal 37 (1999) 66–72.
[22] M.P. Patel, E. Reshotko, D. Hyman, Microfabricated shear-stress sensors, part 3: reducing calibration uncertainty, AIAA Journal 40 (2002) 1582–1588.
[23] J. Zhe, V. Modi, K.R. Farmer, A microfabricated wall shear-stress sensor with capacitative sensing, Journal of Microelectromechanical Systems 14 (2005) 167–175.
[24] V. Chandrasekharan, J. Sells, J. Meloy, D. Arnold, M. Sheplak, A metal-on-silicon differential capacitive shear stress sensor, Solid-State Sensors, Actuators and Microsystems Conference, Transducers (2009) 1537–1540.
[25] V. Chandrasekharan, J. Sells, J. Meloy, D.P. Arnold, M. Sheplak, A Microscale differential capacitive direct wall-shear-stress sensor, Journal of Microelectromechanical Systems 20 (2011) 622–635.
[26] A.A. Barlian, S. Park, V. Mukundan, B.L. Pruitt, Design and characterization of microfabricated piezoresistive floating element-based shear stress sensors, Sensors and Actuators A: Physical 134 (2007) 77–87.

[27] J. Shajii, K. Ng, M.A. Schmidt, A microfabricated floating-element shear stress sensor using wafer-bonding technology, Journal of Microelectromechanical Systems 1 (1992) 89–94.
[28] F.M. White, Viscous Fluid Flow, 3rd ed., Tata McGraw-Hill Education, New York, 1974.
[29] G.G. Zilliac, T.H. Pulliam, M.B. Rivers, J. Zerr, M. Delgado, N. Halcomb, H. Lee, A comparison of the measured and computed skin friction distribution on the common research model, in: 49th AIAA Aerospace Sciences Meeting, AIAA 2011-1129, 2011.
[30] Y. Chen, E. Reshotko, Study of flow around a MEMS shear-stress sensor element, in: 54th Annual Meeting of the Division of Fluid Dynamics of the American Physical Society, 2001.
[31] Analog Devices, 24-Bit Capacitance to Digital Converter with Temperature Sensor, Rev 0, 2007.
[32] J. Luo, A. Flewitt, S. Spearing, N. Fleck, W. Milne, Young's modulus of electroplated Ni thin film for MEMS applications, Materials Letters 58 (2004) 2306–2309.